ADVANCED HEALTHCARE MATERIALS
www.advhealthmat.de

Manipulating ICG *J*-Aggregation and Disaggregation for Imaging-Guided Cancer Therapy with Self-Reporting Efficiency

*Zhicong Chao, Kun Wu, Jiahui Sun, Mengchen Wang, Huangxian Ju, and Ying Liu**

Integrating imaging guided therapy and therapeutic effect self-reporting would highly benefit clinic applications. *J*-type aggregates of organic dyes with corresponding photothermal effect have made them popular agents for photoacoustic (PA) imaging and photothermal therapy (PTT). However, approaches to manipulate the disaggregation of *J*-aggregate with corresponding organic dye fluorescence recovery have rarely been reported, which limits the full exploration of *J*-aggregate in therapeutic applications. Herein, indocyanine green (ICG) *J*-aggregate is designed in a micelle structure (*J*-ICG-Micelle) by co-assembling ICG with DSPE-Pep-PEG, which contains peptide KADEVDAC that recognized and cleaved by caspase-3. Taking advantages of the red-shifted absorbance of *J*-ICG-Micelle, it achieves PA imaging navigated delivery process with an indication of tumor accumulation time and position to perform PTT. Corresponding cell apoptosis and caspase-3 generation cleaves peptide KADEVDAC and results in fluorescence recovery of ICG, which self-reports therapeutic effect in real time, and the intensity for fluorescence recovery demonstrates similar tendency as H&E staining at tumor sections. The as-presented *J*-ICG-Micelle would have a promising contribution to precise cancer therapy.

1. Introduction

The dynamic progress of tumor development and individual heterogeneity of cancer patients affect therapeutic efficiency.[1] Integrating therapy implementation part and imaging part for tracing systematic circulation and in situ evaluating therapeutic efficiency would highly benefit clinic applications. However, current therapeutic effect evaluation techniques such as magnetic resonance imaging (MRI),[2] computed tomography (CT),[3] usually rely on tumor volume measurements,[4] and thus are delayed in reporting time. In addition, they usually require separated injections of apoptosis reagent and contrast agent as "post-treatment" evaluation approaches, which complicates operation process.[5]

J-aggregates are formed by self-assembly of organic dyes through π-π dispersive interactions or electrostatic interactions.[6] Though usually causing fluorescence quenching, the as-obtained *J*-type aggregates acquire other new properties such as largely enhanced absorbance[7] and corresponding photothermal effect,[8] which make them popular photoacoustic[9] (PA) contrast agents[10] with good performance in PA imaging[11] guided photothermal therapy (PTT).[12] Many strategies have been developed for in situ generation of *J*-aggregate in tumor microenvironment for surgical navigation[13] and phototherapy,[14] but approaches and corresponding trigger molecules for activatable *J*-aggregate disaggregation have rarely been approached,[15] which limited the full exploration of *J*-aggregates in therapeutic applications. Responsive disaggregation of *J*-aggregates with fluorescence signal recovery would endow *J*-aggregate based therapeutic system with *in-situ* cell apoptosis reporting capability, which integrates imaging guided therapy with early-evaluation of therapeutic efficiency, and would enable timely adjustment of treatment plans to enhance therapeutic efficiency and reduce overtreatment or side effect.

Caspases are a family of intracellular cysteine proteases, which play important roles in the initiation and execution of apoptosis.[16] Caspase-3 functions as a key effector of cell death and has emerged as a unique and specific target for apoptosis imaging.[17] Current intracellular and in vivo caspase-3 imaging techniques mostly rely on regulating intramolecular charge transfer (ICT) process[18] or fluorescence resonance energy transfer (FRET) process between a fluorescent dye and caspase-3 substrate peptide,[19] or manipulating caspase-3 specific cleavage of substrate peptide and corresponding intracellular macrocyclization-mediated self-assembly of contrast agents to nano-aggregates with imaging signal changes.[20] However, it is challenging to couple current caspase-3 imaging strategies[21]

Z. Chao, K. Wu, J. Sun, M. Wang, H. Ju, Y. Liu
State Key Laboratory of Analytical Chemistry for Life Science
School of Chemistry and Chemical Engineering
Nanjing University
Nanjing210023, China
E-mail: yingliu@nju.edu.cn
Y. Liu
Chemistry and Biomedicine Innovation Center
Nanjing University
Nanjing210023, China

The ORCID identification number(s) for the author(s) of this article can be found under https://doi.org/10.1002/adhm.202405032

DOI: 10.1002/adhm.202405032

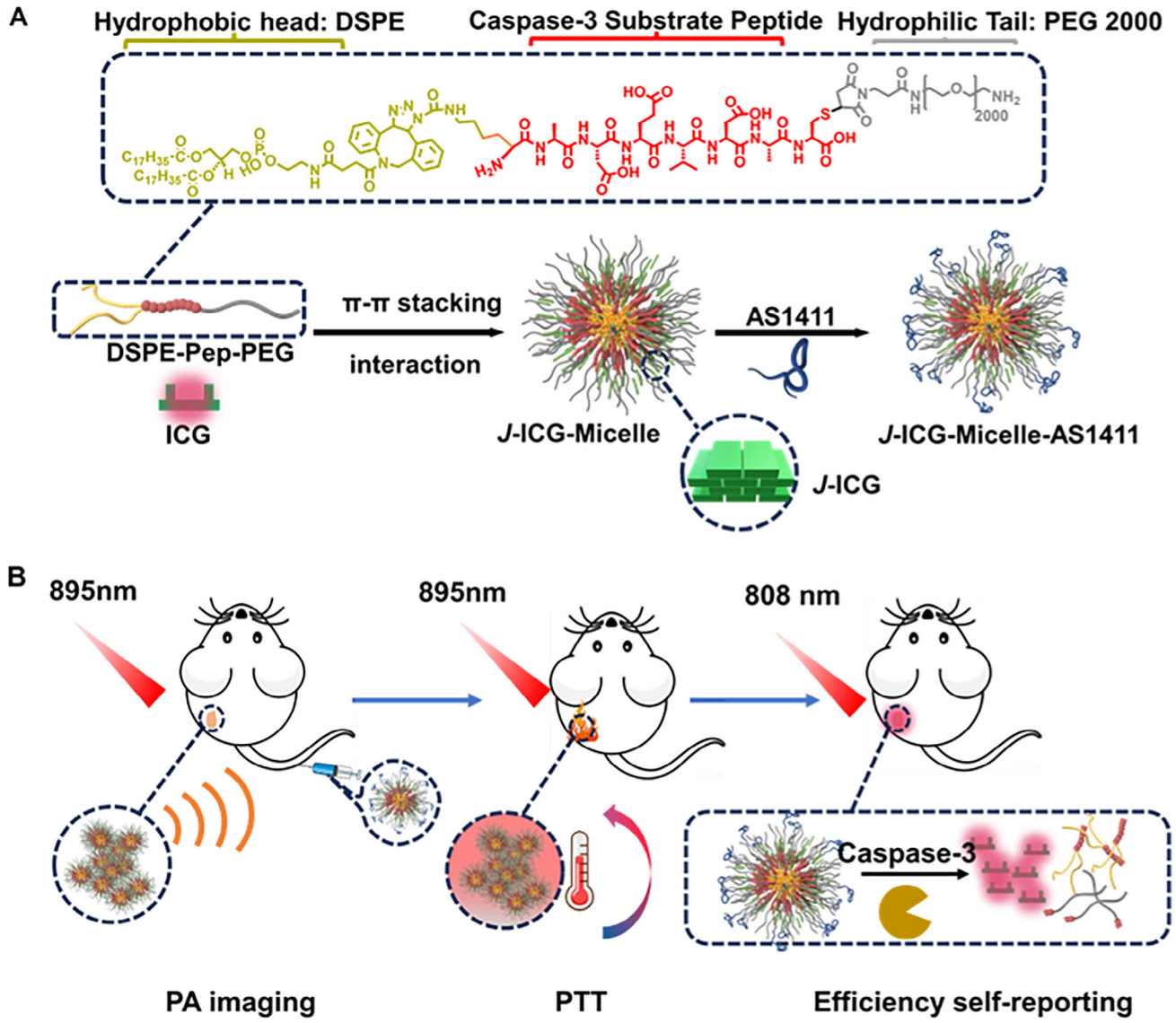

Scheme 1. Schematic illustration of A) *J*-ICG-Micelle-AS1411 synthesis and B) PA imaging guided PTT with NIR-II fluorescence recovery for in situ therapeutic efficiency self-reporting.

with therapeutic platform[22] for *in-situ* therapeutic efficiency self-evaluation.

Indocyanine green (ICG) is a NIR cyanine dye with good water solubility that approved by FDA for clinical application,[23] here we design a strategy to manipulate the *J*-aggregation of ICG and caspase-3 responsive disaggregation, which achieves photoacoustic imaging-guided photothermal therapy (PTT) with *in-situ* reporting of therapeutic effect via NIR-II fluorescence recovery. ICG is self-assembled with a synthesized amphiphilic polymer DSPE-Pep-PEG to generate ICG *J*-aggregate in a micelle structure (*J*-ICG-Micelle). As the skeleton for micelle structure, DSPE-Pep-PEG contains a hydrophobic head DSPE, peptide KADEVDAC that is recognized and cleaved by caspase-3, and a hydrophilic tail PEG2000 (**Scheme** 1A, DSPE-Pep-PEG). DSPE-Pep-PEG is self-assembled to micelle structure, and ICG co-assembles with DSPE-Pep-PEG to obtain *J*-ICG that anchored inside micelle to obtain *J*-ICG-Micelle (Scheme 1A, *J*-ICG-Micelle). Attributing to the π-π stacking of ICG hydrophobic backbone and electrostatic interaction between sulfonate group located at the side chain of ICG and amine group located at PEG terminus, *J*-ICG remained stable structure in micelle. Aptamer AS1411 with carboxyl functional group is further conjugated to *J*-ICG-micelle via amidation with PEG terminus amine group, which specifically recognizes nucleolin at cancer cell membrane and intracellularly delivers the as-obtained *J*-ICG-micelle-AS1411 (Scheme 1A, J-ICG-Micelle-AS1411).

The red shifted absorbance of *J*-ICG-micelle-AS1411 to NIR region endows it good photothermal effect and photoacoustic imaging capability. *J*-ICG-micelle-AS1411 shows strong PA signal under 895 nm excitation, which navigates particle in vivo delivery and indicates the time and tumor grown position to perform PTT (Scheme 1B, PA imaging). PTT is performed under 895 nm

excitation for 10 min (Scheme 1B, PTT), which causes cell apoptosis and generates caspase-3 intracellularly. Caspase-3 cleaves peptide KADEVDAC, and breaks micelle skeleton DSPE-Pep-PEG with the degradation of *J*-ICG-Micelle-AS1411, which leads to the disaggregation of *J*-ICG with recovery of ICG fluorescence for *in-situ* evaluation of therapeutic effect (Scheme 1B, efficiency self-reporting). The level of cell apoptosis and therapeutic efficiency corresponding to different PTT duration time are verified with caspase-3 assay kit and H&E staining at tumor sections, which demonstrate similar tendencies as the extents of ICG NIR-II fluorescence recovery. The as-presented *J*-ICG-micelle with caspase-3 responsive *J*-ICG disaggregation integrates imaging guided therapy and early-stage *in-situ* therapeutic effect evaluation, therefore would have promising contribution to precise cancer therapy.

2. Results and Discussion

2.1. Synthesis of *J*-ICG-Micelle

As the skeleton to construct micelle structure, amphiphilic molecule DSPE-Pep-PEG contained a hydrophobic head DSPE, a caspase-3 recognizing substrate peptide KADEVDAC and a hydrophilic tail PEG. Mal-PEG-NH_2 (Mw ≈2000) was conjugated to terminus cysteine of N_3-KADEVDAC (Mw = 932.97) via thiol-maleimide reaction to obtain N_3-Pep-PEG-NH_2 (**Figure 1A**, N_3-Pep-PEG-NH_2). The as-obtained N_3-Pep-PEG-NH_2 was verified by MALDI mass spectrometry with molecular mass of 3016.11 (Figure S1A, Supporting Information). N_3-Pep-PEG-NH_2 was further reacted with DSPE-DBCO via click reaction to obtain DSPE-Pep-PEG-NH_2 (Figure 1A, DSPE-Pep-PEG-NH_2). The as-obtained DSPE-Pep-PEG-NH_2 was purified by dialysis, and verified by MALDI mass spectrometry with molecular mass of 4073.23 (Figure S1B, Supporting Information). N_3-Pep-PEG-NH_2 demonstrated azide characteristic peaks at 2101 cm^{-1} in FTIR spectrum, which disappeared for DSPE-Pep-PEG-NH_2 (Figure 1B), further confirming the successful conjugation of DSPE-DBCO to N_3-Pep-PEG-NH_2. Furthermore, the High-performance liquid chromatography (HPLC) results indicated that the purity of the N_3-Pep-PEG-NH_2 after dialysis was 93.2%, while that of the DSPE-Pep-PEG-NH_2 was 91.5%.(Figure S1D, Supporting Information)

The as-obtained DSPE-Pep-PEG-NH_2 was mixed with ICG, and self-assembled into micelle structure. ICG *J*-aggregate was formed in the as-obtained micelle structure, therefore showed a strong and narrow absorption peak at 895 nm (Figure 1C, Absorbance, *J*-ICG-Micelle), which was obviously red-shifted compared with the absorption peak of ICG monomer (788 nm) (Figure 1C, Absorbance, ICG), confirming the successful generation of ICG *J*-aggregate in micelle structure. The as-obtained *J*-ICG-Micelle showed a spherical structure with a diameter of 20.2 ± 1.5 nm (Figure 1D), hydration diameter of 23.7 ± 1.2 nm and zeta potential of −20.3 ± 0.09 mV due to the sulfonyl groups contained in ICG (Figure 1E, *J*-ICG-Micelle). In the absence of ICG, DSPE-Pep-PEG-NH_2 still self-assembled to micelle structure with similar hydrated particle of 28.8 ± 2.3 nm and more positive zeta potential of 20.93 ± 0.6 mV. The electrostatic interaction between sulfonyl group of ICG and amino group at PEG terminus play important roles for the organized arrange of ICG molecules to form *J*-aggregate in the as-obtained *J*-ICG-Micelle. Mixing ICG with uncharged DSPE-Pep-PEG or negatively charged DSPE-Pep-PEG-COOH all showed similar hydrated particle size with *J*-ICG-Micelle (Figure S2A, Supporting Information), but their absorbance peaks were similar to that of ICG monomer (Figure S2B, Supporting Information), which indicated the failure to generate *J*-ICG structure. The aggregate peak grew with time and formed a sharp peak with red shifted absorbance at 6 h of mixture solution incubation. Sharp absorbance peak with red-shifted absorbance is determined as the evidence for formation of *J-aggregate* (Figure S2C, Supporting Information). *J*-ICG-Micelle generation process was further studied by keeping DSPE-Pep-PEG at micelle critical concentration of 40 μg mL^{-1}, and changing ICG concentration from 10 to 50 μg mL^{-1}, and *J*-aggregate sharp red-shifted peak was observed at ICG concentration of 35 μg mL^{-1} (Figure S2D, Supporting Information).

Unlike ICG monomer which demonstrated intense fluorescence in 810–1200 nm range (Figure 1C, Fl, ICG), *J*-ICG-Micelle barely showed fluorescence due to aggregation-caused quenching (ACQ) effect which is due to non-radiative pathways in the short-range molecular interactions, such as π–π stacking originating from the planarity of the molecular skeleton[24] (Figure 1C, Fl, *J*-ICG-Micelle). By measuring ICG monomer fluoresence decrease corresponding to DSPE-Pep-PEG-NH_2 concentration, *J*-ICG-Micelle critical concentration was determined as 40 μg mL^{-1} with ICG fluorescence mostly quenched (Figure S3, Supporting Information).

The fluorescence quench of ICG therefore enhanced its photothermal conversion efficiency. *J*-ICG-Micelle dispersed solutions demonstrated concentration dependent temperature increase corresponding to the time of 895 nm laser irradiation (0.8 w cm^{-2}), and resulted in ≈50.7 °C of temperature increase for 100 μg mL^{-1} *J*-ICG-Micelle upon 8 min of irradiation (Figure 1F, 100 μg mL^{-1}). In comparison, pure water only demonstrated ≈6.5 °C of temperature increase in response to same duration and power density of 895 nm laser irradiation. Five cycles of irradiation on/off process showed a consistent photothermal conversion capability with little decay (Figure 1G), and the photothermal conversion efficiency was calculated as 32.2% (Figure S4A, Supporting Information). Generation of *J*-ICG aggregate quenched ICG fluorescence and impaired PDT efficiency (Figure S4C, Supporting Information), thus the most adsorbed energy would convert to heat. In comparison, free ICG didn't show much temperature increase upon 808 nm laser irradation (Figure 1G; Figure S5, Supporting Information, ICG). The amount of ICG encapsulated in micelle was calculated by disaggregating *J*-ICG-Micelle with tween, and measuring the absorbance of released ICG (Figure S6, Supporting Information). Encapsulation efficiency and loading capacity for *J*-ICG-Micells were correspondingly obtained as 87.5% and 75.3% respectively.

2.2. Disassembly Regulation of *J*-ICG-Micelle

Self-assembled micelle is susceptible to many factors such as surfactant[26] and enzyme[27], resulting in micelle disassembly. To verify the absorbance and fluorescence emission change corresponding to *J*-ICG-Micelle disassembly, *J*-ICG-Micelle was incubated with tween, which demonstrated fluorescence recovery in

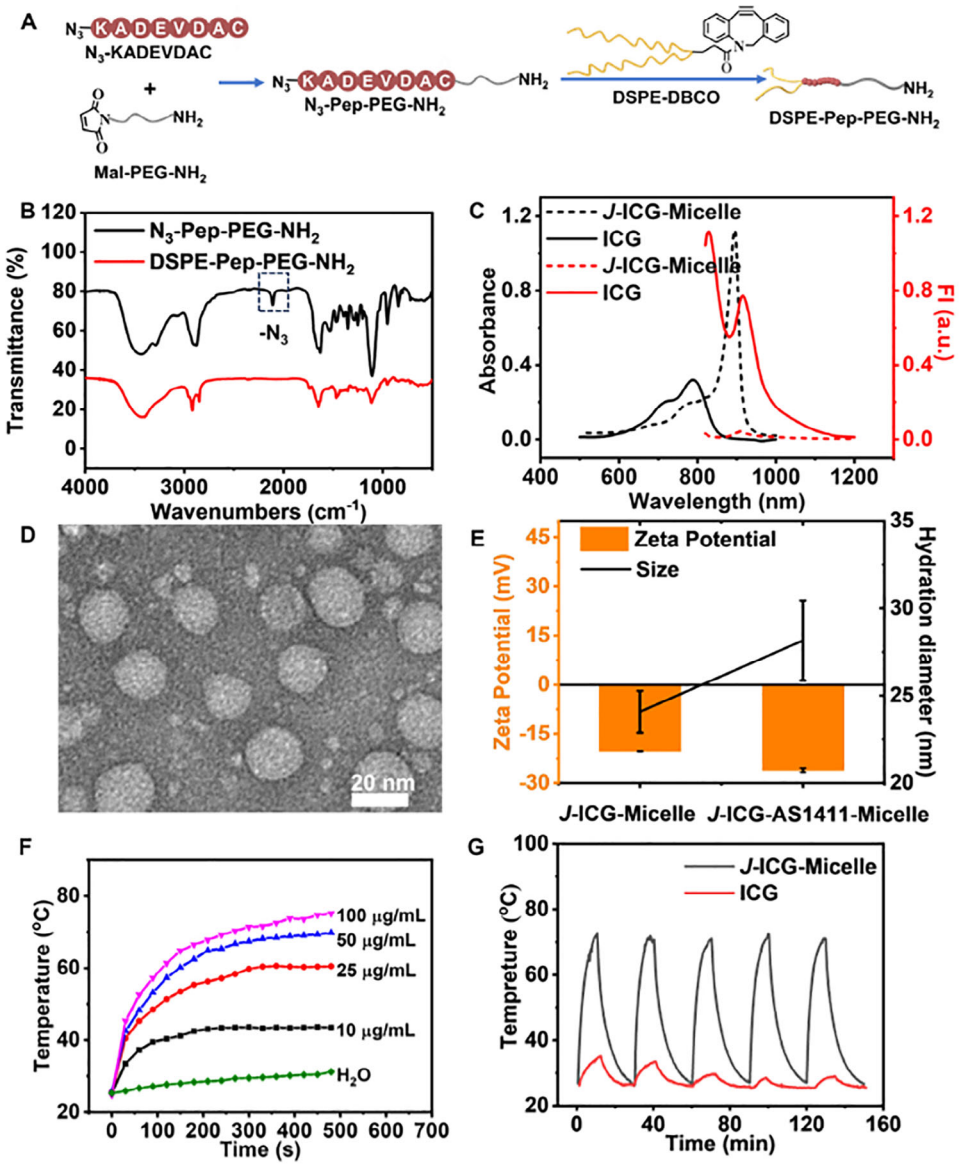

Figure 1. A) Schematic illustration for the synthesis process of DSPE-Pep-PEG-NH_2. B) FTIR characterization of N_3-Pep-PEG-NH_2 and DSPE-Pep-PEG-NH_2. C) Absorption spectra (black) and fluorescence spectra (red) of the ICG monomer (solid line) and *J*-ICG-Micelle (dash line) under 808-nm excitation. D) TEM image of *J*-ICG-Micelle. E) Zeta potentials and hydration diameter of *J*-ICG-Micelle and *J*-ICG-Micelle-AS1411. F) Temperature change of different concentrations *J*-ICG-Micelle dispersed aqueous solution under 895-nm laser irradiation (0.8 W·cm^{-2}). The error bars in (E) indicate means ± S.D. ($n = 3$). G) Temperature profiles of *J*-ICG-Micelle at 100 μg·mL^{-1} and free ICG at 50 μg·mL^{-1} under 5 cycles of laser on/off (0.8 W·cm^{-2},895-nm laser for *J*-ICG-Micelle; 808-nm laser for free ICG).

810–1200 nm range in accompany with suppression of *J*-ICG characteristic absorbance peak at 895 nm (Figure S7, Supporting Information).

As the component for *J*-ICG-Micelle, peptide KADEVDAC was cleaved by caspase-3, which separates DSPE-Pep-PEG-NH_2 to hydrophobic portion AC-PEG-NH_2 and hydrophilic portion DSPE-KADEVD, and demonstrated their corresponding peaks with molecular mass of 1783.21 and 2279.17 respectively in MALDI-TOF-MS (Figure S8A, Supporting Information). Therefore, incubating *J*-ICG-Micelle with caspase-3 resulted in the disassembly of *J*-ICG-Micelle with degradation of *J*-ICG to ICG monomer (**Figure** 2A). DLS also demonstrated a gradual increase of hydration diameter from 21.03 nm to 1802.21 nm up to 3 h of caspase-3 incubation (Figure 2B; Figure S8B, Supporting Information), indicating the sufficient degradation of *J*-ICG-Micelle and corresponding generation of large-sized aggregates. Upon 4 h of incubation with caspase-3, the micelle structure was completely deformed on TEM (Figure S8C, Supporting Information). Incubating caspase-3 with *J*-ICG-Micelle demonstrated time dependent decrease of *J*-ICG characteristic absorption peak at 895 nm, in accompany with a gradual increase of ICG monomer characteristic absorption peak at 780 nm (Figure 2C) and characteristic

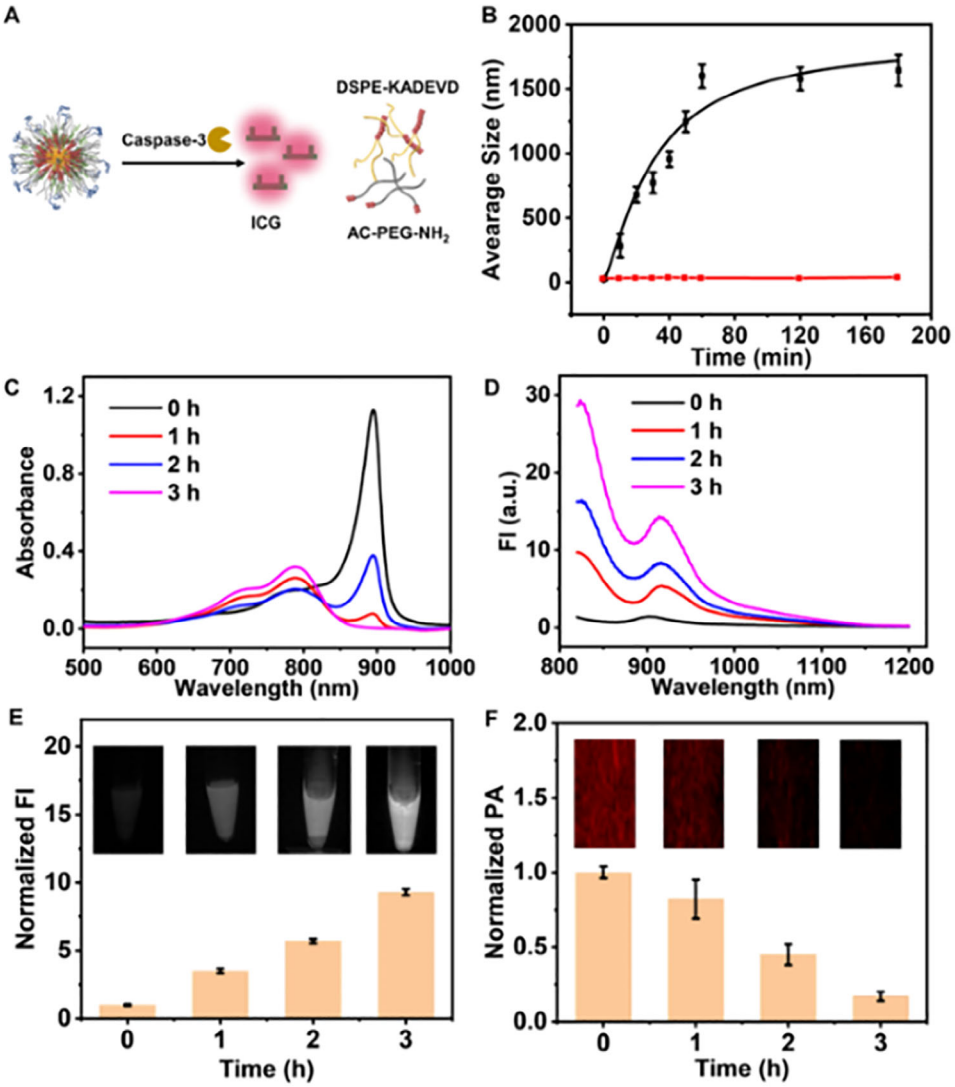

Figure 2. A) Schematic illustration of Caspase-3 responsive *J*-ICG-Micelle disassembly. B) Kinetic degradation curve of *J*-ICG-Micelle (black) and Ns-*J*-ICG-Micelle (red) incubating with caspase-3, Time corresponding C) Absorption spectra and D) fluorescence spectra of *J*-ICG-Micelle upon caspase-3 incubation time. E) NIR-II fluorescence intensity with 1150 nm long pass filter and F) PA imaging intensity of *J*-ICG-Micelle in response to caspase-3 incubation time. The inset in (E), (F) are corresponding in vivo fluorescence images and PA images. The error bars in (B),(E) and (F) indicate means ± S.D. (n = 3).

fluorescence peak at 910 nm (Figure 2D). Upon 4 h incubating with caspase-3, the recovery of 910 nm fluorescence was ≈15.2-fold compared with that of *J*-ICG-Micelle (Figure 2D), confirming the efficient disassembly of *J*-ICG-Micelle in response to caspase-3. Though its maximum fluorescence emission was located in NIR-I region at 910 nm, ICG also showed appreciable fluorescence intensity in NIR-II region, which demonstrated gradually increased fluorescence intensity under imaging system equipped with 1150 nm long pass filter (LP1150) (Figure 2E). Photoacoustic signal demonstrated contrary tendency with time dependent intensity diminishing at 895 nm due to the decrease of characteristic absorbance at 895 nm in accompany with *J*-ICG-Micelle disassembly (Figure 2F)

To verify the reaction specificity of caspase-3-induced *J*-ICG-Micelle disassembly, nonspecific *J*-ICG-Micelle (Ns-*J*-ICG-Micelle) was prepared by the self-assembly of ICG with DSPE-nsPep-PEG-NH_2 (Figure S1C, Supporting Information, nsPep indicates peptide with scrambled sequence that couldn't be recognized by caspase-3, KADVEDAC) and set as negative control. With the absence of caspase-3 substrate peptide DEVD participating in the micelle assembly process, Ns-*J*-ICG-Micelle remained integral when incubating with caspase-3, and didn't show absorbance red-shift (Figure S9A, Supporting Information) nor fluorescence recovery at 910 nm (Figure S9B, Supporting Information). Different nonspecific proteases, including caspase-9, cathepsin-B, MMP-2, trypsin, and detection solution without caspase-3, were also incubated with *J*-ICG-Micelle respectively under the same condition as caspase-3, but none of them showed fluorescence recovery (Figures S10 and S11, Supporting Information). The specific and sensitive NIR-II fluorescence change in

response to caspase-3 guaranteed the application of *J*-ICG-Micelle for therapeutic effect evaluation.

2.3. Synthesis of *J*-ICG-Micelle-AS1411 and its Photothermal Effect

DNA aptamer AS1411 specifically recognizes nucleolin that overexpressed on cancer cell membrane,[25] thus carboxyl functionalized AS1411 (AS1411-COOH) was conjugated to *J*-ICG-Micelle surface NH_2 group via amidation to achieve active targeting of cancer cells. The as-obtained *J*-ICG-Micelle-AS1411 demonstrated increased hydrodynamic diameter to 28.4 ± 2.3 nm and decreased zeta potential to −26.1 ± 0.6 mV (Figure 1E, *J*-ICG-micelle-AS1411).

To confirm the conjugation of AS1411 to *J*-ICG-Micelle, Cy3 labelled AS1411 was used to prepare *J*-ICG-Micelle-AS1411$_{Cy3,}$ which clearly demonstrated Cy3 fluorescence (Figure S12, Supporting Information). The as-obtained *J*-ICG-Micelle-AS1411$_{Cy3}$ was incubated with MCF-7 cells, which showed strong intracellular Cy3 fluorescence (Figure S13, Supporting Information *J*-ICG-micelle-AS1411$_{Cy3}$, MCF-7). On the contrary, *J*-ICG-Micelle$_{Cy3}$ in the absence of AS1411 incubated MCF-7 cells barely showed intracellular fluorescence (Figure S13, Supporting Information *J*-ICG-micelle-AS1411$_{Cy3}$, MCF-7). *J*-ICG-Micelle-AS1411$_{Cy3}$ incubated MCF-10A cells that in the absence of nucleolin expression barely showed intracellular fluorescence either (Figure S13, Supporting Information *J*-ICG-micelle-AS1411$_{Cy3}$, MCF-10A). *J*-ICG-Micelle-AS1411 incubated MCF-7 cells also demonstrated much stronger photoacoustic signal intensity compared with *J*-ICG-Micelle-AS1411 incubated MCF-7 cells and *J*-ICG-Micelle-AS1411 incubated MCF-10A cells (Figure S14, Supporting Information). These results indicated specific recognition and intracellular delivery of *J*-ICG-Micelle-AS1411 to MCF-7 cells.

The internalization of 100 μg mL^{-1} *J*-ICG-Micelle-AS1411 and Ns-*J*-ICG-Micelle-AS1411 resulted in cell viability of 87.43% (Fig 3A, NIR(-)) and 94.33% (Fig S15) respectively, indicating good biocompatibility. The photothermal effect of *J*-ICG-Micelle-AS1411 in response to NIR irradiation resulted in cell apoptosis, and showed concentration dependent decrease in cell viability (Fig 3A, NIR(+)). Cell viability was decreased to only 25.9% for 100 μg mL^{-1} *J*-ICG-Micelle-AS1411 incubated cells, demonstration good PTT effect. Caspase-3 was generated in cell apoptosis process, which disassembled *J*-ICG-Micelle-AS1411 in accompany with ICG fluorescence recovery. Intracellular ICG fluorescence demonstrated time dependent increase and saturated at 135 min after the exertion of PTT (Fig 3B), indicating the capability of *J*-ICG-Micelle-AS1411 for in situ monitoring cell apoptosis after the implementation of treatment. To verify the specificity of intracellular ICG fluorescence recovery corresponding to caspase-3 generation, MCF-7 cells were treated with paraformaldehyde after PTT, and incubated with caspase-3 antibody that labelled with Cy5 dye (anti-casp-3-Cy5) to visualize intracellular caspase-3 generation. Cy5 fluorescence and ICG fluorescence were well overlapped intracellularly from *J*-ICG-Micelle-AS1411 treated MCF-7 cells under NIR irradiation (**Figure** 3C, group 1), indicating the accuracy of ICG fluorescence for cell apoptosis indication. On the contrary, *J*-ICG-Micelle-AS1411 incubated MCF-7 cells in the absence of NIR irradiation had no PTT effect, therefore didn't show intracellular ICG fluorescence nor Cy5 fluorescence (Figure 3C, group 2). Ns-*J*-ICG-Micelle-AS1411, which has a random peptide amino acid sequence nonspecific to caspase-3 was also incubated with MCF-7 cells and irradiated with NIR light, it demonstrated Cy5 fluorescence intracellularly due to the successful execution of PTT with caspase-3 generation. However, ICG fluorescence recovery was barely observed since caspase-3 could not recognize nonspecific peptide and incapable to disassemble Ns-*J*-ICG-Micelle-AS1411 (Figure 3C, group 3; Figure S16, Supporting Information).In order to verify the universality of *J*-ICG-Micelle-AS1411 photothermal therapy effect and the evaluation of therapeutic effect, relevant experiments were conducted on MDA-MB-231 cells and SK-BR-3 cells respectively. The expressions of Caspase-3 in three cell lines including MCF-7, MDA-MB-231, and SK-BR-3 were similar, and the corresponding intracellular NIR fluorescence recoveries were also consistent (Figure S17, Supporting Information). To verify the applicability of *J*-ICG-Micelle-AS1411 for in vivo monitoring caspase-3 generation, MCF-7 cells that seeded in well plates were treated under similar conditions, and the corresponding NIR-II fluorescence signal recovery and PA signal suppression were monitored. Time-dependent NIR-II fluorescence increase (Figure S16, Supporting Information, group 1) and PA signal decrease (Figure S18, Supporting Information, group 1) were respectively observed from *J*-ICG-Micelle-AS1411 incubated MCF-7 cells under NIR irradiation. *J*-ICG-Micelle-AS1411 incubated MCF-7 cells without NIR irradiation and Ns-*J*-ICG-Micelle-AS1411 incubated MCF-7 cells with NIR irradiation barely showed a single change neither for NIR-II fluorescence (Figure S16, Supporting Information, group 2,3) nor PA imaging (Figure S18, Supporting Information, group 2,3).

To demonstrate the proportional intracellular ICG fluorescence recovery to caspase generation, MCF-7 cells that incubated with *J*-ICG-Micelle-AS1411 were treated with different concentrations of caspase-3 inhibitor KADEVDAC to prevent caspase-3 activity after PTT. Intracellular ICG fluorescence gradually decreased corresponding to inhibitor concentration. The as-treated MCF-7 cells were also incubated with anti-casp-3-Cy5 to verify caspase-3 expression, and the corresponding Cy5 fluorescence demonstrated a similar tendency as that of ICG (Figure S19, Supporting Information), indicating the capability of *J*-ICG-Micelle-AS1411 in quantifying intracellular caspase-3 generation.

In addition, MCF-7 cells that were incubated with *J*-ICG-Micelle-AS1411 were irradiated with NIR light for different periods from 5 to 15 min to represent different therapeutic effects, and the fluorescence changes for cell groups were imaged via confocal microscopy. The intensity of intracellular ICG fluorescence recovery (Figure 3D) and PA signal suppression (Figure 3E) were both proportional to PTT time, indicating enhanced caspase-3 generation according to PTT duration time. MTT assay and flow cytometry assay were also used to evaluate the therapeutic effect, which demonstrated a gradual decrease of cell viability (Figure S20, Supporting Information) and increase of cell apoptosis rate (Figure 3F) according to PTT duration time. Intracellular ICG fluorescence recovery and PA imaging signal suppression demonstrated similar tendencies as that of cell apoptosis, indicating *J*-ICG-Micelle-AS1411 was capable of reporting therapeutic effect in real time.

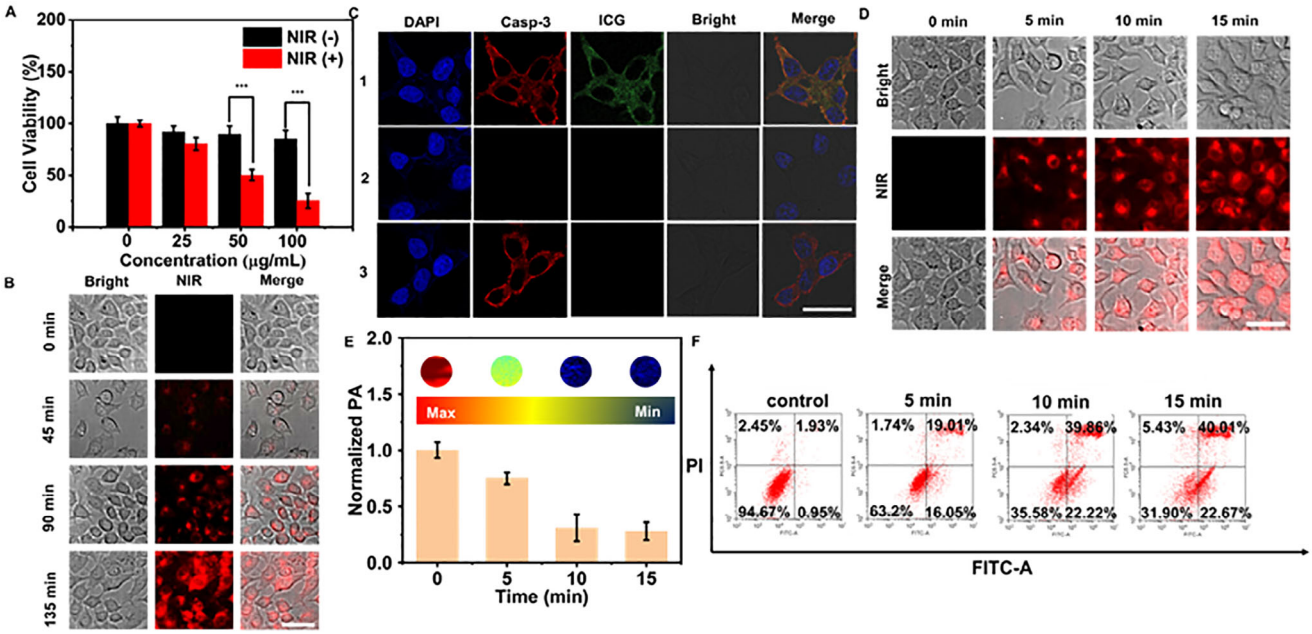

Figure 3. A) Viability of MCF-7 cells incubated with different concentrations of *J*-ICG-Micelle-AS1411 in the presence (NIR(+)) and absence (NIR(-)) of NIR irradiation; B) Intracellular NIR-II fluorescence recovery at different time after PTT. The microscopy images were collected with 808 nm excitation wavelength and 900–1700 nm as the detection window. The scale bar is 50 μm; C) CLSM images of MCF-7 cells incubated with anti-casp-3-Cy5 and 1) *J*-ICG-Micelle-AS1411 with PTT, 2) *J*-ICG-Micelle-AS1411 without PTT, 3) Ns-*J*-ICG-Micelle-AS1411 with PTT. The scale bar is 25 μm; D) Intracellular NIR-II fluorescence recovery, E) PA signal intensity, and F) Flow cytometry analysis for *J*-ICG-Micelle-AS1411 incubated MCF-7 cells corresponding to different PTT duration times. Measurements in (D)-(F) were performed at 2 h post PTT. The scale bar in (D) is 50 μm.The inset in (E) indicated PA imaging of *J*-ICG-Micelle-AS1411 incubated MCF-7 cells corresponding to different PTT duration times. The error bars in (A), (E) indicate means ± S.D. (n = 3), ***p < 0.001, Student's *t*-test.

2.4. *J*-ICG-Micelle-AS1411 for Imaging Guided PTT with In Vivo Therapeutic Effect Evaluation

MCF-7 tumor-bearing mice were used for the application of *J*-ICG-Micelle-AS1411 for PA imaging guided PTT with in situ NIR-II fluorescence recovery for therapeutic effect evaluation. The accumulation of *J*-ICG-Micelle-AS1411 at tumor grown position was monitored via PA imaging after tail vein injection, which demonstrated a time-dependent signal increase at the tumor position with a maximum signal intensity achieved at 12 h post injection (**Figure** 4A; Figure S22A, Supporting Information). In contrast, saline-injected mice showed no photoacoustic signal (Figure 4A). *J*-ICG-Micelle-AS1411$_{Cy3}$ was further administrated to MCF-7 tumor-bearing mice for visualization micelle delivery, which also demonstrated effective accumulation of micelle at tumor at 12 h post administration (Figure S21, Supporting Information), indicating efficient in vivo tumor targeting of *J*-ICG-Micelle-AS1411. Therefore 12 h post intravenous injection was chosen as the ideal time point for exerting PTT.

12 MCF-7 tumor-bearing mice were randomly divided into four groups and intravenously injected with 1) saline; 2) *J*-ICG-Micelle-AS1411 without NIR irradiation; 3) *J*-ICG-Micelle-AS1411 with NIR irradiation; and 4) Ns-*J*-ICG-Micelle-AS1411 with NIR irradiation respectively. The temperature profiles of the mouse tumors were recorded to demonstrate the in vivo photothermal effect of *J*-ICG- Micelle-AS1411. Compared with saline injected mice group, 10 min of PTT raised local temperatures to 53.5 °C for *J*-ICG-Micelle-AS1411 injected mice group (Figure 4B; Figure S22B, Supporting Information). The *J*-ICG-Micelle-AS1411 treated mice group with NIR irradiation showed gradual increase of NIR-II fluorescence post PTT with maximum signal intensity reached at 8 h post injection (Figure 4C; Figure S22C, Supporting Information, group 3), indicating efficient in situ disassembly of *J*-ICG-Micelle-AS1411. Metabolism of the released ICG monomer also resulted in the gradual brightening of liver. On the contrary, the *J*-ICG-Micelle-AS1411 treated mice in the absence of NIR irradiation barely showed NIR-II fluorescence in tumor grown position due to the incapability of caspase-3 generation (Figure 4C; Figure S22C, Supporting Information, group 2). Ns-*J*-ICG-Micelle-AS1411 didn't respond to caspase-3, therefore didn't demonstrate fluorescence recovery at tumor grown position either (Figure 4C; Figure S22C, Supporting Information, group 4). These results confirmed the specific disassembly of *J*-ICG-Micelle-AS1411 in response to PTT with in situ NIR-II fluorescence recovery. PA imaging also showed gradual decrease of *J*-ICG-Micelle signal under 895 nm excitation and increase of ICG signal under 808 nm excitation for *J*-ICG-Micelle treated mice post PTT (Figure S23, Supporting Information, *J*-ICG-Micelle-AS1411), while Ns-*J*-ICG-Micelle treated mice group with NIR irradiation only showed slightly decreased PA imaging signal intensity probably due to micelle metabolism post PTT (Figure S23, Supporting Information, Ns-*J*-ICG-Micelle-AS1411). These results confirmed the specific disassembly of *J*-ICG-Micelle in response to PTT. Immunofluorescence staining of caspase-3 was also collected from tumor slices, which showed strong Caspase-3 fluorescence from *J*-ICG-Micelle-AS1411 treated mice group

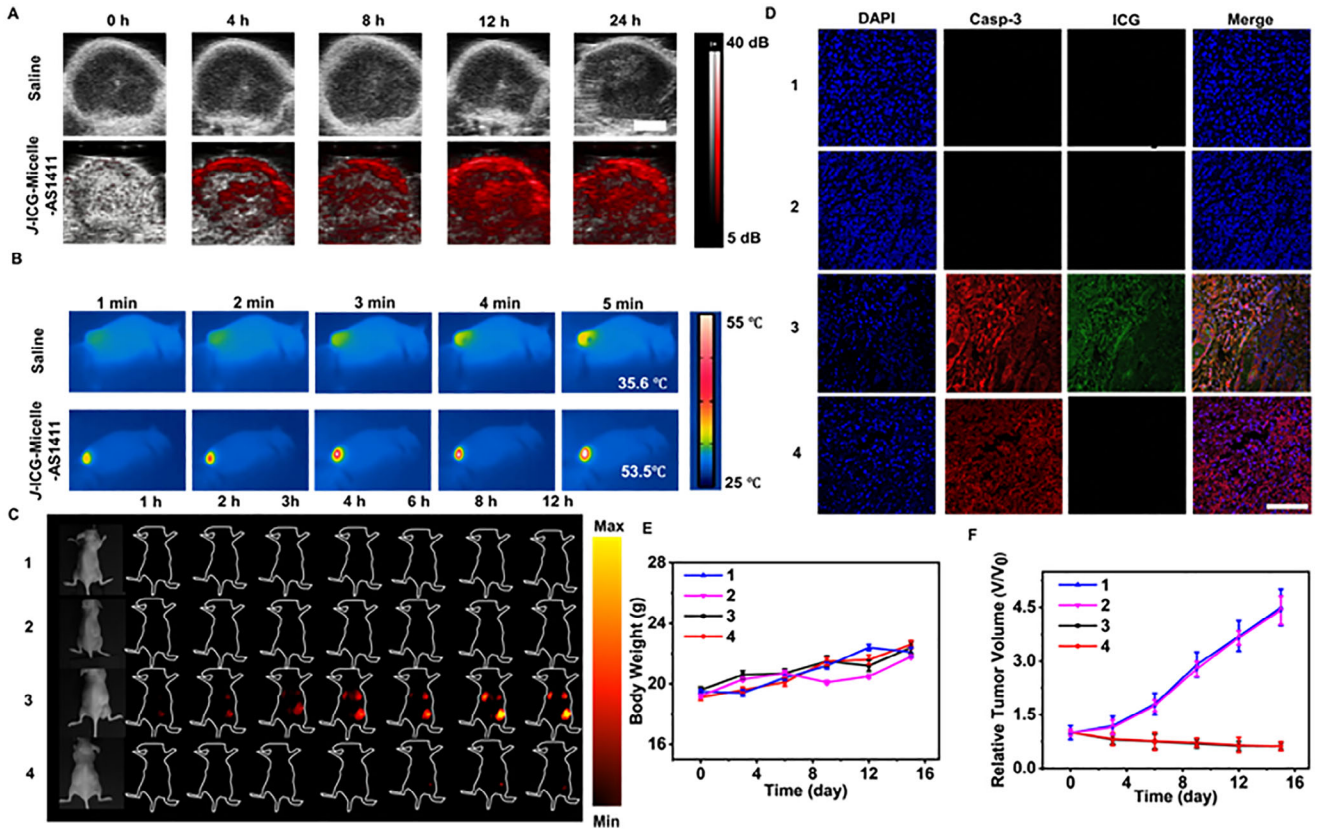

Figure 4. A) Time-dependent tumor site photoacoustic images (red-white scale) of the MCF-7 tumor-bearing mice intravenously injected with saline *J*-ICG-Micelle-AS1411. The tumor boundaries were delineated by ultrasound images (gray scale). The scale bar in (A) is 20 mm. B) In vivo NIR thermography of the tumors from MCF-7 tumor-bearing mice intravenously injected with saline and *J*-ICG-Micelle-AS1411 at different time points after 895 nm laser irradiation. C) Time-dependent in vivo NIR-II fluorescence imaging, D) Immunofluorescence staining images, E) Body weight, and F) Tumor growth curves for MCF-7-tumor-bearing mice administrated with 1) Saline, 2) *J*-ICG-Micelle-AS1411 without NIR irradiation, 3) *J*-ICG-Micelle-AS1411 with NIR irradiation, 4) Ns-*J*-ICG-Micelle-AS1411 with NIR irradiation. The scale bar in (D) is 75 μm. The error bars in (E) and (F) indicate means ± S.D. (n = 3).

with NIR irradiation and Ns-*J*-ICG-Micelle-AS1411 treated group with NIR irradiation (Figure 4D, group 3, 4, Caspase-3), indicating the effective caspase-3 generation upon PTT. In the absence of NIR irradiation, *J*-ICG-Micelle-AS1411 treated mice didn't demonstrate PTT effect, therefore barely showed caspase-3 immunofluorescence (Figure 4D, group 2, Caspase-3). ICG fluorescence was also monitored from tumor slice to verify its capability for *in-situ* therapeutic effect evaluation, which showed obvious fluorescence on tumor slice for *J*-ICG-Micelle-AS1411 treated mice with NIR irradiation (Figure 4D, group 3, ICG), but no ICG fluorescence for *J*-ICG-Micelle-AS1411 treated group without NIR irradiation (Figure 4D, group 2, ICG) nor Ns-*J*-ICG-Micelle-AS1411 treated group with NIR irradiation (Figure 4D, group 4, ICG). This result indicated in vivo ICG fluorescence recovery was capable of in situ evaluating therapeutic effect.

All the mice groups didn't show weight loss during the treatment period (Figure 4E), and H&E staining demonstrated no damage to the major organs of the mice after treatment (Figure S24, Supporting Information), indicating good biocompatibility of J-ICG-Micelle-AS1411 with little biotoxicity for in vivo application. Considering their similar photothermal effect that was confirmed by the same levels of temperature increase in response to laser irradiation (Figure S25, Supporting Information), both *J*-ICG-Micelle-AS1411 treated mice group and Ns-*J*-ICG-Micelle-AS1411 treated mice group under NIR irradiations for PTT showed effective suppression of tumor growth (Figure 4F, group 3,4; Figure S26A, Supporting Information, group 3,4). Severe tumor damage was also observed from H&E staining (Figure S26B, Supporting Information, H&E, group 3,4) and TUNEL staining (Figure S26B, Supporting Information, TUNEL, group 3,4) respectively from the slice of tumor for *J*-ICG-Micelle-AS1411 treated mice group and Ns-*J*-ICG-Micelle-AS1411 treated mice group with PTT.

3. Conclusion

In this study, *J*-ICG-Micelle was synthesized by co-assembling ICG with DSPE-Pep-PEG to form a micelle structure, which provided good photothermal property for PA imaging guided PTT. Cell apoptosis generated caspase-3, which cleaved peptide in DSPE-Pep-PEG and resulted in the disintegration of *J*-ICG-Micelle with NIR-II fluorescence recovery of ICG for self-reporting of therapeutic effect. The as-presented *J*-ICG-Micelle with caspase-3 responsive *J*-ICG disaggregation integrated

imaging guided therapy and early stage in-situ therapeutic effect evaluation, which has potential application prospect in precise therapy.

4. Experimental Section

Synthesis of N_3-Pep-PEG-NH_2: NH_2-PEG-Mal (Mw = 2000, 2 mg, 1 µmol) and N_3-KADEVDAC (10 mg, 10 µmol) were dissolved in 10 mL PBS (pH = 7.5) and shaked at 37 °C for 2 h. The as-obtained N_3-Pep-PEG-NH_2 was collected by centrifugation, further purified by extensively dialyzing (interception molecular weight of 1000) against deionized water to remove unreacted peptide, and obtained as white powder (2.2 mg, yield 73.3%) after lyophilization. MALDI-TOF verified molecular mass of as-obtained N_3-Pep-PEG-NH_2 as 3016.11.

Synthesis of DSPE-Pep-PEG-NH_2: The above obtained DSPE-DBCO (100 mg, 0.1 mmol) and N_3-Pep-PEG-NH_2 (450 mg, 0.15 mmol) were dissolved in 30 mL $CHCl_3$, stirred at 37 °C for 8 h. After removed solvent by vacuum distillation, water was added to the precipitate and ultrasonicated for dispersion. The as-obtained solution was dialyzed (interception molecular weight of 2000) overnight to get DSPE-Pep-PEG-NH_2 as white powder (273 mg, yield 70.7%) after lyophilization. MALDI-TOF verified molecular mass of as-obtained DSPE-Pep-PEG-NH_2 as 4073.23 [M+Na].

Preparation of J-ICG-Micelle: ICG (0.5 mg) and the above prepared DSPE-Pep-PEG-NH_2 (1 mg) were co-dissolved in ultrapure water (10 mL), heated to 80 °C and kept for 2 h with vigorous stirring, and continuously stirred at room temperature for 8 h to generate micelle structure that encapsulated with ICG *J* aggregate. The as-obtained J-ICG-micelle was concentrated by ultrafiltration and stored at −4 °C for further use. Control micelle, NsPep-J-ICG-micelle was also prepared by self-assembling ICG with DSPE-Pep-PEG-NH_2 which contained scrambled peptide (KADVEDAC).

The encapsulation efficiency value was calculated by the following formula:

$$\text{encapsulation efficiency} = \frac{w_1}{w_2} \times 100\% \quad (1)$$

where w_1 is the mass of the ICG monomer in the *J*-ICG-micelle, and w_2 is the mass of the total ICG monomer in the reaction.

The loading capacity value was calculated by the following formula:

$$\text{loading capacity} = \frac{w_1}{w_3} \times 100\% \quad (2)$$

where w_1 is the mass of the ICG monomer in the *J*-ICG-micelle, and w_3 is the mass of the total *J*-ICG-micelle.

Preparation of J-ICG-Micelle-AS1411: *J-ICG*-micelle was functionalized with AS1411 for targeting nucleolin at cancer cell membrane. *J*-ICG-micelle dispersed water (1.5 mg mL^{-1}, 1.0 mL), EDC/NHS aqueous solution (1.5 M, 0.3 mL), AS1411-COOH aqueous solution (200 µM, 50 µL) were mixed in HEPES buffer (0.5 M, pH = 7.5), stirred at room temperature for 3 h, ultra-filtrated to remove unreacted AS1411-COOH, and obtained *J*-ICG-micelle-AS1411.

Caspase-3 mediated disaggregation of *J*-ICG-micelle-AS1411 was verified by mixing it (10 µg mL^{-1}, dispersed in 95 µL 50 mM PIPES containing 100 mM NaCl, 1 mM EDTA, 0.1% w/v CHAPS, 25% w/v sucrose, pH = 7.2) with recombinant caspase-3 (0.01 µg $µL^{-1}$, 5 µL). The reaction mixture was incubated at room temperature for 60 min, then diluted to a total volume of 300 µL with deionized water for NIR fluorescence recovery measurement. The solution was excited at 808 nm, and the emission was collected from 820 to 1200 nm.

Photothermal Effect of J-ICG-Micelle-AS1411: The above-prepared *J*-ICG-micelle-AS1411 aqueous dispersed solutions (100 µg mL^{-1}, 1 mL) were irradiated with 895 nm laser (0.8 W•cm^{-2}) for 10 min. Temperatures of *J*-ICG-micelle-AS1411 dispersed solutions were measured with an accuracy of 0.1°C with a thermocouple probe every 30 s.

To measure the photothermal conversion efficiency (η), the temperature change of the *J*-ICG-micelle-AS1411 dispersion was recorded as a function of time under continuous 895 nm laser irradiation with a 0.8 W cm^{-2} power density until the solution reached a steady state temperature. The η value was calculated by the following formula. The η value was calculated by the following formula:

$$\eta = \frac{hS\left(T_{max} - T_{sur}\right) - Q_s}{I\left(1 - 10^{-A}\right)} \quad (3)$$

where h is the heat transfer coefficient, S is the surface area of the container, and the value of hS is gained from Figure S4 (Supporting Information). Tmax is the equilibrium temperature, Tsurr is the ambient temperature of the surroundings, Q_S is expressed as the heat associated with the light absorbance, I is the incident laser power and A is the absorbance of the *J*-ICG-Micelle at 895 nm.

Verification Intracellular Delivery of J-ICG-Micelle-AS1411 and Intracellular Generation of Caspase-3: To trace the intracellular distribution of *J*-ICG-micelle-AS1411, Cy3-AS1411-COOH was used to synthesize *J*-ICG-micelle-AS1411-Cy3. MCF-7 cells and MCF-10A cells were cultured in the chambers at 37 °C and 5% CO_2. After 80% confluence, the adherent cells were washed twice with 1×PBS. *J*-ICG-micelle-AS1411-Cy3 (100 µg mL^{-1}, 100 µL) was then added to the chamber. For co-localization with cell nucleus, the cells were incubated with DAPI for 10 min at room temperature followed by washed once with 1×PBS. The cells were kept at RPMI 1640 for 30 min and imaged on CLSM with 550 nm excitation for Cy3, and DAPI was co-localized with 405 nm excitation.

To visualize intracellular generation of caspase-3, MCF-7 cells were first incubated with different concentrations of *J*-ICG-micelle-AS1411 for 4 h, then irradiated with 895 nm laser for 10 min, and incubated for 2 h. MCF-7 cells were first fixed with 3.7% formaldehyde in 1×PBS at room temperature, washed twice with cold 1×PBS, and permeabilized with 0.1% Triton X-100 in 1×PBS. The cells were further blocked with 2% BSA in 1×PBS for 30 min and washed twice with 1×PBS, incubated with polyclonal Caspase-3 antibody (antibody/PBS, v/v = 1/99) overnight at 4 °C, washed with 1×PBS, then incubated with mouse anti-Caspase-3 Rabbit pAb, (mouse anti-Caspase-3 Rabbit pAb/PBS, v/v = 1/99) for 1 h, washed with 1×PBS again. Caspase-3 was imaged on CLSM with 645 nm excitation for the fluorescence from Cy5 dye labelled anti-Caspase-3 Rabbit pAb and 690 nm excitation for ICG fluorescence recovery. DAPI was co-localized with 405 nm excitation.

Real-Time Intracellular Imaging of Cell Apoptosis: MCF-7 cells were cultured in the twenty-four -well chambers at 37 °C. After 80% confluence, the adherent cells were washed twice with 1×PBS. *J*-ICG-micelle-AS1411 (100 µg mL^{-1}, 100 µL) was then added to the chamber, and incubated at 37 °C for 2 h. The cells were washed twice with 1×PBS, exposed under 895 nm laser irradiation (0.8 W cm^{-2}) ≈10 min for PTT. After continuously incubating in RPMI 1640 medium for different times (45 min, 90min and 135 min), ICG fluorescence recovery was observed using optical microscope at 910 nm with 808 nm excitation. To verify the level of ICG fluorescence recovery for different therapeutic levels, different concentrations of *J*-ICG-micelle-AS1411 (25, 50, 100 µg mL^{-1}, 100 µL) were incubated with MCF-7 and irradiated with 895 nm laser for 10 min. The corresponding ICG fluorescence recovery for different concentrations *J*-ICG-micelle-AS1411 treatments were evaluated by optical microscope with the same procedure above. MCF-7 cells that only exposed with 895 nm laser in the absence of *J*-ICG-micelle-AS1411 was set as control.

MTT Assay and Verification of Cell Apoptosis: MTT assay was performed to verify cell apoptosis corresponding to different concentrations *J*-ICG-micelle-AS1411 treatments. MCF-7 cells were plated in a 96-well plate at 37 °C and 5% CO_2 for 24 h. The culture medium was replaced with RPMI 1640 containing different concentrations (25, 50, 100 µg mL^{-1}, 100 µL) of *J*-ICG-micelle-AS1411, and continuously incubated at 37 °C with 5% CO_2 for an additional 24 h respectively. 50 µL of 1×MTT reagent was then added to each well and the plate was kept at 37 °C for 4 h. The medium was then removed and 100 µL of DMSO was added to each well followed by shaking

for 10 min. The cell viability was calculated by measuring the ratio of 490 nm characteristic absorbance for treated cells over untreated cells.

Flow Cytometry and Verification of Cell Apoptosis: Flow cytometry was performed to verify cell apoptosis corresponding to different concentrations *J*-ICG-micelle-AS1411 treatments. MCF-7 cells were plated in a 24-well plate at 37 °C and 5% CO_2 for 24 h. The culture medium was replaced with RPMI 1640 containing different concentrations (25, 50, 100 µg mL^{-1}, 1.0 mL) of *J*-ICG-micelle-AS1411. Next, the cells were applied to 895 nm laser irradiation (0.8 W cm^{-2}, 10 min) and further cultured for 24 h (37 °C, 5% CO_2). The cells apoptosis and necrosis analysis were determined by Annexin V-FITC Apoptosis Detection Kit and flow cytometry.

In Vitro Photoacoustic Imaging: Endra Nexus128 PA tomography system (Endra Inc., Ann Arbor, Michigan) was used for PAI study. The system houses a tunable nanosecond pulsed laser (7 ns pulses, 72 angels, 5pulse/angel, 2.36 mJ/pulse on the animal surface), wavelength range (680–900 nm), 128 unfocused ultrasound transducers (with 5 MHz center frequency and 3 mm diameter) arranged in a hemispherical bowl filled with water, sample tray on top of the bowl, data acquisition/reconstruction console, servo motors for 3D rotation of the bowl, and a temperature monitor of the water bath. Typically, *J*-ICG-Micelle (10 µg) in caspase assay buffer was incubated with caspase-3 (1 µg mL^{-1}) at 37 °C for different time. After the reaction, the solutions were load into a length of fine bore polythene tube (0.86 mm ID, 1.27 mm OD), and the tubes were then sealed. The tubes were fixed at the bottom of the hemispherical bowl and the PA images were captured at 895 nm.

In Vivo PTT: All in vivo experiments were approved by the Animal Ethical and Welfare Committee of Nanjing University with approval number of IACUC-2209004. The mice type was female nude BALB/c mice which aged 6–8 weeks and weighted 16–18g. The mice were purchased from Cavens Laboratory Animal Technology Co., Ltd., acclimated and tested for infectious diseases for 1 week, and subcutaneously injected with MCF-7 cells (1×10^7 cells each mouse) at the flank region. When the tumor size reached ≈200 mm^3, the mice were randomly divided into four groups (3 mice in each group) and intravenously injected with (1) saline; (2) 100 µL *J*-ICG-micelle-AS1411 with ICG equivalent concentration of 0.5 mg mL^{-1}; (3) 100 µL NsPep-*J*-ICG-micelle-AS1411 with ICG equivalent concentration of 0.5 mg mL^{-1}; (4) 100 µL *J*-ICG-micelle-AS1411 with ICG equivalent concentration of 0.5 mg mL^{-1} respectively. When the injected micelle accumulated at tumor grown position at ≈12 h post intravenous injection, groups (3) and (4) were irradiated with 895 nm light irradiation (0.8 W cm^{-2}) for 10 min. After therapeutic treatments, the body weights and tumor volumes for all mice groups were kept measured every three days for 15 days with formula: Volume = (Length×$Width^2$)/2. The mice were sacrificed at day 15th, and major organs, together with tumors were removed, fixed in 4% formalin and then processed for hematoxylin and eosin (H&E) staining studies for pathological features.

In Vivo Photoacoustic Imaging: To perform in vivo delivery navigation via photoacoustic imaging (PAI), the mice that injected with *J*-ICG-micelle-AS1411 were exposed to 895 nm laser irradiation at different time points post-injection, and ultrasound/PA signals were detected by the transducer.

After continuous 10 min 895 nm light irradiation (0.8 W cm^{-2}) for PTT, PAI was performed again at tumor grown positions at 1 h, 4 h, and 8 h. PA signals of ICG *J*-aggregate were measured with excitation wavelengths of 895 nm respectively to demonstrate caspase-3 responsive micelle degradation.

In Vivo NIR-II Fluorescence Imaging: After continuous 10 min 895 nm light irradiation (0.8 W cm^{-2}) for PTT, NIR-II fluorescence imagings were recorded at 1150 nm for tumor grown positions at designed time points (1, 2, 3, 4, 6, 8 and 12 h).

Statistical Analysis: Partial data undergoes normalization processing. All data were presented as mean ± standard and analysed using IBM SPSS Statistics 30.0.0 by Student's *t*-test, as detailed in the figure captions. *P*-values < 0.05 were considered significant, with levels of significance indicated as: $*P < 0.05$; $**P < 0.01$; $***P < 0.001$; $****P < 0.0001$. Quantification and statistics for each experiment were derived from three independent samples or three independent experiments unless otherwise specified in the legends.

Supporting Information

Supporting Information is available from the Wiley Online Library or from the author.

Acknowledgements

The authors gratefully acknowledge the National Natural Science Foundation of China (22374073).

Conflict of Interest

The authors declare no conflict of interest.

Data Availability Statement

The data that support the findings of this study are available from the corresponding author upon reasonable request.

Keywords

caspase-3 imaging, ICG J-aggregate, NIR-II imaging, photothermal therapy, self-reporting therapeutic efficiency

Received: January 15, 2025
Revised: April 19, 2025
Published online:

[1] F. Wang, N. Sun, Q. Li, J. Yang, X. Yang, D. Liu, *J. Am. Chem. Soc.* **2022**, *145*, 919.
[2] H. Liu, Y. Guo, J. Lv, J. Xu, Q. Zhang, G. Guan, C. Zhang, C. Lu, Q. Gong, C. Liang, D. Xu, G. Song, *Adv. Funct. Mater.* **2025**, *35*, 2412848.
[3] M. Shabsigh, L. A. Solomon, *Chem. Biomed. Imaging.* **2024**, *2*, 615.
[4] C. Kuhl, *Radiology* **2007**, *244*, 356.
[5] S. Kataria, J. Qi, C.-W. Lin, Z. Li, E. L. Dane, A. M. Iyer, J. Sacane, D. J. Irvine, A. M. Belcher, *ACS Nano* **2023**, *17*, 17908.
[6] N. M. D. Jasmina Hranisavljevic, G. A. Wurtz, G. P. Wiederrecht, *J. Am. Chem. Soc.* **2002**, *124*, 4536.
[7] a) J. Liu, X. Zhang, M. Fu, X. Wang, Y. Gao, X. Xu, T. Xiao, Q. Wang, Q. Fan, *Biomater. Sci.* **2023**, *11*, 7124; b) D. H. Thanippuli Arachchi, U. Barotov, C. F. Perkinson, T. Šverko, A. E. K. Kaplan, M. G. Bawendi, *ACS Nano* **2024**, *18*, 20422.
[8] a) R. Liu, J. Tang, Y. Xu, Y. Zhou, Z. Dai, *Nanotheranostics* **2017**, *1*, 430; b) Y. Xu, X. Meng, Y. Zhao, M. Jia, H. Zhu, J. Song, Y. Su, W. Qiao, J. Qi, Z. Y. Wang, *ACS Appl. Mater. Interfaces* **2024**, *16*, 39005; c) Y. Zhu, F. Wu, B. Zheng, Y. Yang, J. Yang, H. Xiong, *Nano Lett.* **2024**, *24*, 8287.
[9] H. Zhang, M. Wu, F. A. N. Sumadi, C. Fu, Q. Meng, M. Alanazi, Z. Zhang, Z. P. Xu, H. T. Ta, R. Zhang, *Adv. Funct. Mater.* **2025**, *35*, 2414788.
[10] a) H. Liu, X. Wang, Y. Huang, H. Li, C. Peng, H. Yang, J. Li, H. Hong, Z. Lei, X. Zhang, Z. Li, *ACS Appl. Mater. Interfaces* **2019**, *11*, 30511; b) S. Wu, W. Zhang, C. Li, Z. Ni, W. Chen, L. Gai, J. Tian, Z. Guo, H. Lu, *Chem. Sci.* **2024**, *15*, 5973.
[11] J. Ye, Z. Li, Q. Fu, Q. Li, X. Zhang, L. Su, H. Yang, J. Song, *Adv. Funct. Mater.* **2020**, *30*, 2001771.
[12] C. Shao, F. Xiao, H. Guo, J. Yu, D. Jin, C. Wu, L. Xi, L. Tian, *iScience* **2019**, *22*, 229.
[13] Z. Li, P.-Z. Liang, L. Xu, X.-X. Zhang, K. Li, Q. Wu, X.-F. Lou, T.-B. Ren, L. Yuan, X.-B. Zhang, *Nat. Commun.* **2023**, *14*, 1843.

[14] a) H. Dang, D. Yin, Y. Tian, Q. Cheng, C. Teng, Y. Xu, L. Yan, *J. Mater. Chem. B* **2022**, *10*, 5279; b) N. Kwon, G. O. Jasinevicius, G. Kassab, L. Ding, J. Bu, L. P. Martinelli, V. G. Ferreira, A. Dhaliwal, H. H. L. Chan, Y. Mo, V. S. Bagnato, C. Kurachi, J. Chen, G. Zheng, H. H. Buzzá, *Angew. Chem., Int. Ed.* **2023**, *62*, 202305564.
[15] D. Zhai, W. Xu, L. Zhang, Y.-T. Chang, *Chem. Soc. Rev.* **2014**, *43*, 2402.
[16] A. Nancy, Y. L. Thornberry, *Science* **1998**, *281*, 1312
[17] a) M. W. Boudreau, J. Peh, P. J. Hergenrother, *ACS Chem Biol.* **2019**, *14*, 2335; b) A. C. Clark, *Chem. Rev.* **2016**, *116*, 6666; c) H.-W. Liu, L. Chen, C. Xu, Z. Li, H. Zhang, X.-B. Zhang, W. Tan, *Chem. Soc. Rev.* **2018**, *47*, 7140.
[18] a) P. Cheng, Q. Miao, J. Li, J. Huang, C. Xie, K. Pu, *J. Am. Chem. Soc.* **2019**, *141*, 10581; b) J. Fang, Y. Zhao, A. Wang, Y. Zhang, C. Cui, S. Ye, Q. Mao, Y. Feng, J. Li, C. Xu, H. Shi, *Anal. Chem.* **2022**, *94*, 5149; c) J. Liu, F. Wu, M. Wang, M. Tao, Z. Liu, Z. Hai, *Anal. Chem.* **2023**, *95*, 9404.
[19] a) Q. Fu, H. Feng, L. Su, X. Zhang, L. Liu, F. Fu, H. Yang, J. Song, *Angew. Chem., Int. Ed.* **2021**, *61*, 202112237; b) X. Huang, M. Swierczewska, K. Y. Choi, L. Zhu, A. Bhirde, J. Park, K. Kim, J. Xie, G. Niu, K. C. Lee, S. Lee, X. Chen, *Angew. Chem., Int. Ed.* **2012**, *51*, 1625;
[20] a) Z. Chen, M. Chen, K. Zhou, J. Rao, *Angew. Chem., Int. Ed.* **2020**, *59*, 7864; b) Y. Wang, H. Bai, Y. Miao, J. Weng, Z. Huang, J. Fu, Y. Zhang, J. Lin, D. Ye, *Angew. Chem., Int. Ed.* **2022**, *61*, 202200369; c) Y. Wang, X. Hu, J. Weng, J. Li, Q. Fan, Y. Zhang, D. Ye, *Angew. Chem., Int. Ed.* **2019**, *58*, 4886.
[21] T.-I. Kim, H. Jin, J. Bae, Y. Kim, *Anal. Chem.* **2017**, *89*, 10565.
[22] H. Liao, S. Wang, X. Wang, D. Z. Dai, Y. Zhang, C. Zhu, J. Li, *Chem. Biomed. Imaging.* **2024**, *2*, 313.
[23] Z. Hu, C. Fang, B. Li, Z. Zhang, C. Cao, M. Cai, S. Su, X. Sun, X. Shi, C. Li, T. Zhou, Y. Zhang, C. Chi, P. He, X. Xia, Y. Chen, S. S. Gambhir, Z. Cheng, J. Tian, *Nat. Biomed. Eng.* **2020**, *4*, 259.
[24] M. Huang, R. Yu, K. Xu, S. Ye, S. Kuang, X. Zhu, Y. Wan, *Chem. Sci.* **2016**, *7*, 4485.
[25] a) M. Beygi, F. Oroojalian, S. Azizi-Arani, S. S. Hosseini, A. Mokhtarzadeh, P. Kesharwani, A. Sahebkar, *Adv. Funct. Mater.* **2024**, *34*, 2310881; b) Z. Lv, Z. Li, S. Zou, P. Li, N. Song, R. Zhang, M. Xu, M. Liu, F. Li, J. Li, P. Liu, C. Yao, D. Yang, *Adv. Funct. Mater.* **2023**, *34*, 2311069.
[26] Z. Huo, Z. Yu, W. Xu, S. Xu, *The Journal of Physical Chemistry C* **2024**, *128*, 2070
[27] T. C. Hou, Y. Y. Wu, P.-Y. Chiang, K. T. Tan, *Chemical Science* **2015**, *6*, 4643.